

In-plane impedance spectroscopy in aerosol deposited NiMn₂O₄ negative temperature coefficient thermistor films

Jungho Ryu, Dong-Soo Park, and Rainer Schmidt

Citation: *Journal of Applied Physics* **109**, 113722 (2011); doi: 10.1063/1.3592300

View online: <http://dx.doi.org/10.1063/1.3592300>

View Table of Contents: <http://scitation.aip.org/content/aip/journal/jap/109/11?ver=pdfcov>

Published by the AIP Publishing

Articles you may be interested in

[Energetic semiconductor bridge device incorporating Al/MoO_x multilayer nanofilms and negative temperature coefficient thermistor chip](#)

J. Appl. Phys. **115**, 194502 (2014); 10.1063/1.4876264

[Electrical conduction of intrinsic grain and grain boundary in Mn-Co-Ni-O thin film thermistors: Grain size influence](#)

J. Appl. Phys. **110**, 093708 (2011); 10.1063/1.3657772

[Studies of temperature dependent ac impedance of a negative temperature coefficient Mn-Co-Ni-O thin film thermistor](#)

Appl. Phys. Lett. **98**, 242112 (2011); 10.1063/1.3596454


[ac hopping admittance in spinel manganate negative temperature coefficient thermistor electroceramics](#)

J. Appl. Phys. **103**, 113710 (2008); 10.1063/1.2938029


[Combinatorial screening of ternary Ni O – Mn₂ O₃ – Cu O composition spreads](#)

J. Appl. Phys. **98**, 043710 (2005); 10.1063/1.2032613


Frustrated by old technology?



Is your AFM dead and can't be repaired?



Sick of bad customer support?




It is time to upgrade your AFM

Minimum \$20,000 trade-in discount for purchases before August 31st

Asylum Research is today's technology leader in AFM

dropmyoldAFM@oxinst.com



The Business of Science®

In-plane impedance spectroscopy in aerosol deposited NiMn_2O_4 negative temperature coefficient thermistor films

Jungho Ryu,¹ Dong-Soo Park,¹ and Rainer Schmidt^{2,a)}

¹Functional Ceramics Group, Korea Institute of Materials Science (KIMS), 66 Sangnam-Dong, Changwon, Gyeongnam 641-831, South Korea

²Departamento Física Aplicada III, GPMC, Universidad Complutense Madrid, Facultad Ciencias Físicas, 28040 Madrid, Spain

(Received 16 February 2011; accepted 16 April 2011; published online 15 June 2011)

Temperature dependent in-plane impedance spectroscopy measurements were carried out in order to analyze the charge transport properties of functional oxide NiMn_2O_4 negative temperature coefficient thermistor films deposited via aerosol deposition techniques onto glass and Al_2O_3 substrates. The in-plane resistivity (ρ) versus temperature (T) curves of all films were uniform over a large temperature range (180 K to 500 K) and showed the typical exponential power-law behavior associated with variable-range hopping. The ρ - T dependences of annealed and as-deposited films exhibited power-law exponents p of about 0.6 and thermistor constants B in the range of 3500 K to 5000 K. As-deposited films showed higher p values as compared to annealed films. As-deposited films exhibited also increased B values, leading to increased sensitivity of the resistance to temperature changes, whereas annealed films deposited on Al_2O_3 showed the lowest scatter in differentiated ρ - T data and might display superior reliability for temperature sensing applications. © 2011 American Institute of Physics. [doi:10.1063/1.3592300]

I. INTRODUCTION

The cubic spinel compound NiMn_2O_4 (NMO) has been well known for many decades as the basis of negative temperature coefficient (NTC) thermistor materials.^{1–7} The electrical resistance shows a uniform exponential increase with decreasing temperature, which makes the material applicable in industrial temperature sensor or compensator applications.^{8–11} For such applications, different NMO film types or bulk devices with a wide range of dopants are commonly used in order to tune the device performance to the application's requirements.^{12–14} Nevertheless, the pure NMO compound is still the subject of recent research efforts in order to establish new and more efficient synthesis routes^{15–21} and thin and thick film production techniques.^{22–31} Furthermore, the interplay between the physical properties and the Ni and Mn cation distribution on the tetrahedral and octahedral sublattices is still a matter of debate.

In the cubic NMO spinel structure, the close packed oxygen anion sublattice hosts tetrahedral and octahedral interstices, which can both be occupied by Ni and Mn cations. In a regular spinel structure, Ni^{2+} cations would be expected to occupy tetrahedral sites, and Mn^{3+} would occupy octahedral sites. NiMn_2O_4 is not a regular spinel, though, and exhibits a certain degree of inversion. The Ni fraction occupying octahedral sites corresponds to the inversion parameter ν , and 2ν is the fraction of octahedral Mn^{3+} disproportionating into Mn^{2+} and Mn^{4+} , where ν Mn^{2+} occupies tetrahedral sites compensating for ν Ni^{2+} vacancies. In NiMn_2O_4 , ν is usually rather large (0.7 to 0.9), because this is energetically favorable. The disproportionation of a large fraction of the Jahn-

Teller active Mn^{3+} cations releases Jahn-Teller lattice distortions, which leads to an undistorted cubic unit cell.

The temperature dependence of ν and the concomitant variability of the cationic occupancy of tetrahedral and octahedral sites cause the large complexity of this compound, for example, in terms of the magnetic properties, which mainly depend on the exchange interactions of the tetrahedral Mn^{2+} and octahedral Mn^{3+} and Mn^{4+} cations. The charge transport depends on the mixed Mn valence and is based on $\text{Mn}^{3+}/\text{Mn}^{4+}$ hopping on octahedral sites. Tetrahedral Mn^{2+} cations may not contribute to the hopping, because the donation of an electron would leave Mn^{3+} cations on tetrahedral sites, which is unfavourable. Although the temperature dependence of such $\text{Mn}^{3+}/\text{Mn}^{4+}$ hopping is essential for temperature sensing applications, its exact nature is still not fully established. A temperature dependent activation energy for electron hopping was found many decades ago,¹ but only more recently has a theoretically justified small polaron variable-range hopping (VRH) model been employed more frequently.^{32–36}

In this work, we present a detailed in-plane impedance spectroscopy (IS) study on approximately 2 μm thick NMO films produced via the aerosol deposition (AD) technique using glass and Al_2O_3 substrates.²⁸ The recently developed AD technique offers several distinct advantages: it allows highly dense polycrystalline films of sub-micrometer grain size to be produced with a high deposition rate and without an additional sintering densification process.

We show that the AD method is appropriate for producing dense NTC thermistor films with typical NTC resistivity (ρ) versus temperature (T) behavior. The activation energy shows a strong dependence on temperature, and the curves fit well to a VRH power-law model in agreement with previous work^{32–36}.

^{a)}Author to whom correspondence should be addressed. Electronic mail: rainerxschmidt@googlemail.com.

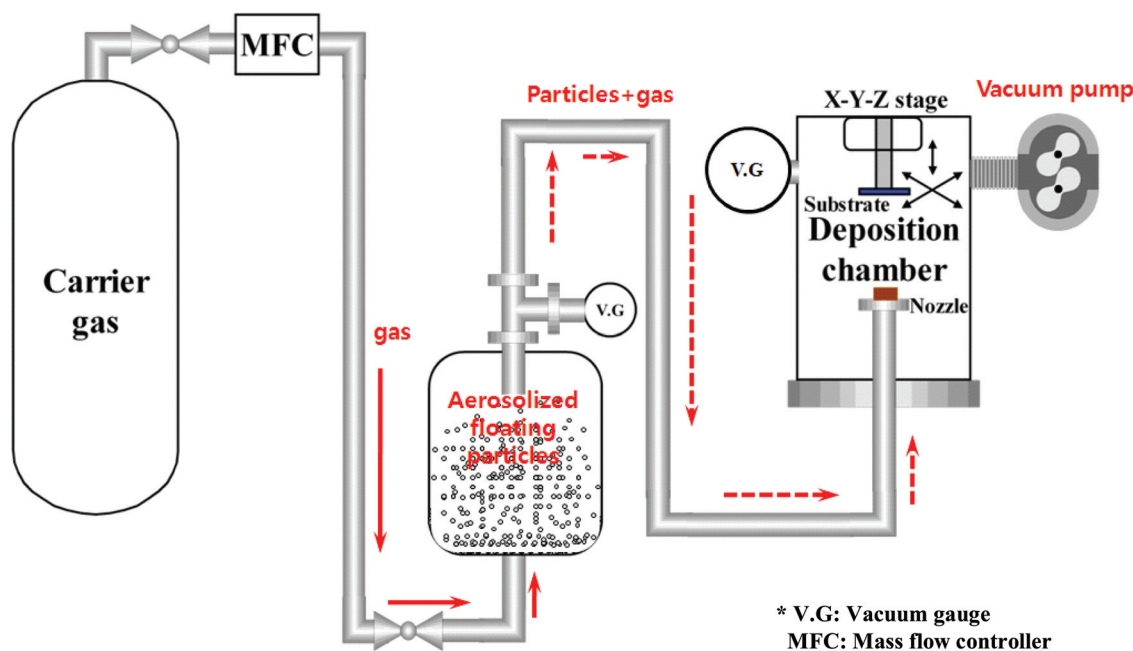


FIG. 1. (Color online) Schematic diagram of the aerosol deposition system.

$$\rho = CT^{2p} \exp\left(\frac{T_0}{T}\right)^p \quad (1)$$

C is a temperature independent factor, T_0 is the characteristic temperature, and p is the power-law exponent.³⁷ In-plane IS proved to be a powerful tool for precisely determining technologically relevant NTC thermistor parameters such as the resistivity ρ ; the thermistor constant B , which is equivalent to the local temperature dependent activation energy ϵ_3 ; and the relative sensitivity of the film thermistor B/T , all over a large temperature range of 180 K to 500 K.

II. EXPERIMENTAL DETAILS

NMO powders were synthesized via the conventional solid state oxide method using reagent grade raw materials of NiO (99.9%, Kojundo Chem. Co., Japan) and Mn₂O₃ (99.9%, Sigma Aldrich Co.). The NiO and Mn₂O₃ powder mixture was ball-milled using high purity 3Y-tetragonal zirconia polycrystalline (TZP) ball media with ethyl alcohol in a high density polyethylene jar for 24 h. The mixed slurry was rotary evaporated and calcined in a high purity alumina crucible in order to facilitate NMO spinel phase formation at 850 °C for 10 h. The calcined NMO powders were confirmed phase pure by X-ray diffraction and were crushed in a planetary mill (Pulverisette 5, Fritsch GmbH, Germany) using 3Y-TZP balls in a ceria stabilized zirconia jar for 10 h in order to obtain an appropriate particle size distribution for AD. The particle size distributions of the powders were characterized using a laser diffraction particle size analyzer (HELOS & RODOS, Windox 5, Sympatec GmbH, Clausthal-Zellerfeld, Germany), and the average particle size (d_{50}) of the calcined powder was $\approx 1.4 \mu\text{m}$.

The NMO powder was mixed with the carrier gas in the aerosol chamber to form an aerosol flow, which was trans-

ported through a tube to a nozzle with rectangular shaped orifices of $5 \times 0.4 \text{ mm}^2$. The flow was accelerated and ejected from the nozzle into a deposition chamber, which was evacuated by a rotary pump with a mechanical booster (see Fig. 1). Medical grade dried air was used as the carrier gas at a flow rate of 5 liters/min. During deposition at room temperature, the pressure in the deposition chamber was monitored as ≈ 1 Torr. The substrate (glass or alumina) was placed 5 mm in front of the nozzle to be exposed to the accelerated NMO particle beam, which formed a dense film on the substrate. Due to rather heavy collisions of NMO particles with the substrate, as well as with the nozzle, the average particle size was crushed down to less than 50 nm, and film formation with dense particle packing was achieved directly from the accelerated NMO particle beam, without an additional post-deposition sintering densification process. This constitutes a major advantage over other polycrystalline film deposition techniques such as screen-printing or tape casting, which both involve organic carrier and binder materials and require post-deposition organic burn-out and densification sintering. The deposition rate was about $0.6 \mu\text{m}/\text{min}$, which is considerably higher than in comparable film deposition processes requiring an evacuated deposition chamber, such as ac sputtering or evaporation techniques. The area of the deposited film was $\approx 5 \times 10 \text{ mm}$, and the film thickness was controlled as $\approx 2 \mu\text{m}$ by the number of repetitions of the nozzle scan. One set of films was loaded into an electric furnace and annealed at 600 °C (glass substrate) or 850 °C (Al₂O₃ substrate) for 1 h.

Two square Ti and two Ag electrodes with a size of $\approx 1 \times 1 \text{ mm}$ and a distance d of approximately 1.5 mm were evaporated onto the film surfaces in order to enable in-plane IS measurements. Figure 2 shows the fractured cross-sectional SEM micrographs of (a) as-deposited NMO film on a glass substrate, (b) 600 °C annealed NMO on glass with Ti

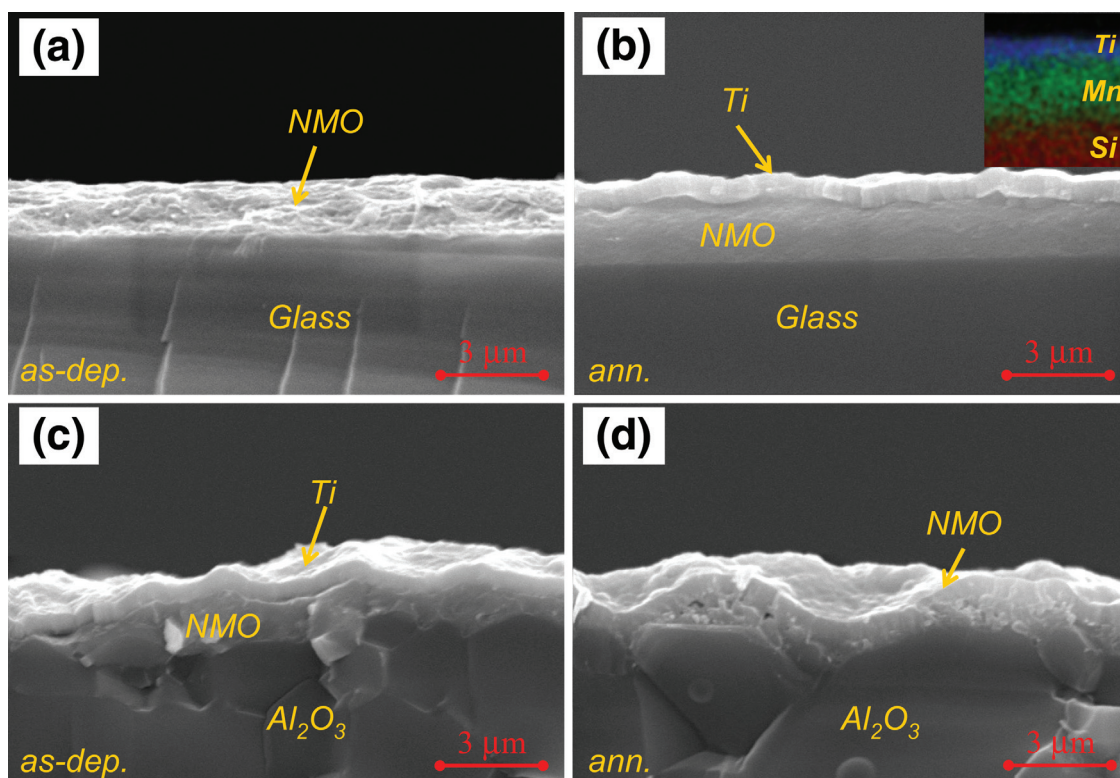


FIG. 2. (Color online) Cross-sectional SEM images of (a) as-deposited NMO film on a glass substrate, (b) 600 °C annealed NMO on glass with Ti electrode (inset: color coded SEM image with elemental contrast for Si, Mn, and Ti), (c) as-deposited NMO on Al_2O_3 with a Ti electrode, and (d) 850 °C annealed NMO on Al_2O_3 .

electrode [inset: film cross-section in elemental contrast mode of a selected area of the same sample applying color coding for Si, Mn, and Ti], (c) as-deposited NMO on Al_2O_3 with a Ti electrode, and (d) 850 °C annealed NMO on Al_2O_3 (JSM-5800, Jeol Co., Tokyo, Japan). The films showed high density, and the Ti electrodes, NMO films, and glass/ Al_2O_3 substrates can be clearly identified. The inset of Fig. 2(b) shows that the 3 different elements are clearly separated, and Ti diffusion into the NMO film and Mn diffusion into the substrates appear to be minimal. No micro-cracks or pores were observed, and all films exhibited good adhesion with the glass/ Al_2O_3 substrates. NMO films on Al_2O_3 substrates exhibited a higher surface roughness, which was inherited from the substrate due to its polycrystalline nature.

For IS measurements, a Novocontrol Alpha-A High Performance Frequency Analyzer equipped with a liquid nitrogen cooled sample chamber was used at 180–500 K. A 100 mV amplitude alternating voltage signal was employed, and IS data were obtained in terms of the real and imaginary parts of the impedance ($Z' - Z''$) between 0.5 Hz and 1 MHz. The data taken from the Ti and Ag electrodes appeared to be identical within experimental error, which indicated that parasitic effects at the sample electrode interfaces were negligible.

III. IMPEDANCE SPECTROSCOPY

A. Basic principles and equivalent circuit fitting

IS experiments have been used extensively in the past in order to analyze the dielectric properties of bulk, single crys-

tal, and film electroceramic materials in detail.^{38–41} IS consists of a time (t)-dependent alternating voltage signal U of angular frequency ω and amplitude U_0 [i.e., $U(\omega, t) = U_0 \cos(\omega t)$] applied to a sample, and effectively the phase shift δ and amplitude I_0 of the current response signal I are measured as $I(\omega, t) = I_0 \cos(\omega t + \delta)$. Because I_0 and δ are time invariant at a given frequency, the impedance is commonly defined as a time-independent complex number $Z^* (= Z' + iZ'')$. The current response of ideal electronic circuit components is (1) in phase with the applied voltage in the case of a resistor R , (2) out of phase by $\delta = -\pi/2$ (-90°) for a capacitor C , and (3) out of phase by $\delta = +\pi/2$ ($+90^\circ$) for an inductor.

In the framework of ideal Debye dielectric relaxations in electroceramic materials, each contribution, such as bulk, grain boundary (GB), or electrode interface relaxations, can be described by an ideal parallel RC element consisting of a resistor and a capacitor in parallel.^{42–44} For the equivalent circuit fitting of experimental IS data, ideal capacitors are often replaced by constant phase elements (CPEs) in order to account for the potential nonideality of the respective relaxation process. Such CPEs show a frequency independent phase shift γ with respect to an ideal capacitor. The macroscopic impedance is the sum of all series RC or R-CPE impedances where each RC/R-CPE element would ideally appear as a separate semicircle in complex plane plots of $-Z''$ versus Z' . A single CPE element and an R-CPE circuit have a complex impedance Z^* of

$$Z_{CPE}^* = \frac{1}{(i\omega)^n C^*}, Z_{R-CPE}^* = \frac{R}{1 + (i\omega)^n R C^*}, \quad (2)$$

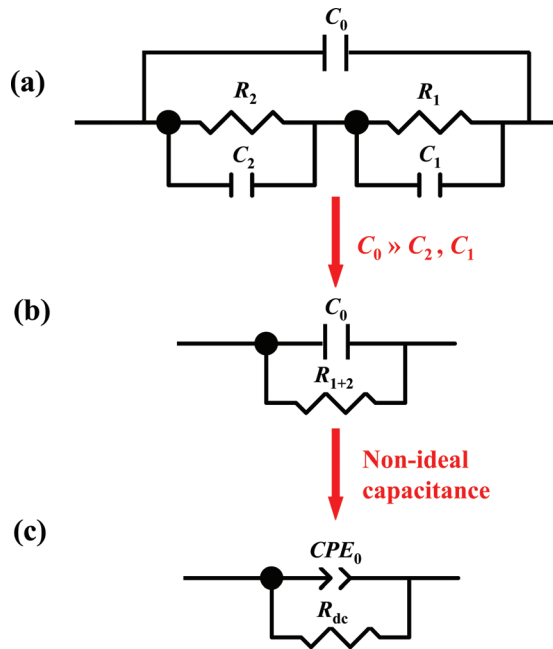


FIG. 3. (Color online) Equivalent circuit for (a) a model sample containing two dielectric relaxations R_1C_1 and R_2C_2 , (b) the specific case of $C_0 \gg C_1/C_2$, and (c) the same case as in (b) but with a nonideal relaxation process.

where R is the resistance, C^* is the capacitance in modified units of Fs^{n-1} , ω is the angular frequency in Hz, n is the critical CPE exponent, and $i = \sqrt{-1}$. The CPE capacitance C^* can be converted into a real capacitance C , given in Faraday, according to a standard procedure.⁴⁵ The critical exponent n equals 1 for an ideal capacitor and has decreasing values below 1 for increasing nonideality, which corresponds to an increasing phase shift γ .

B. Experimental limitations of in-plane IS measurements

In order to demonstrate the limitations of in-plane IS for thin and thick film materials, a model sample with typical dielectric behavior and two distinct dielectric relaxation processes will be considered. In reality, two such relaxations in films may represent the intrinsic film and the extrinsic GB, or the intrinsic film and the extrinsic electrode interface relaxations. In some cases, all 3 contributions (bulk, GB, interface) may be present, but in this model case here we restrict the considerations to two relaxations, one intrinsic (R_1C_1) and one extrinsic (R_2C_2). The two model dielectric relaxations can be represented by two RC elements in series, as depicted in Fig. 3(a).

The most relevant experimental limitation of IS for film in-plane measurements is the stray capacitance of the measurement probe. Such stray capacitance necessarily arises between the measurement cables within the sample probe and the impedance analyzer, and it is referred to as C_0 throughout this work. Its origin implies that for equivalent circuit modeling, the stray capacitance needs to be represented by a capacitor C_0 in parallel to the sample, as is illustrated in Figs. 3(a) and 4. For reliable IS measurements, C_0 should be as low as possible and should be measured before

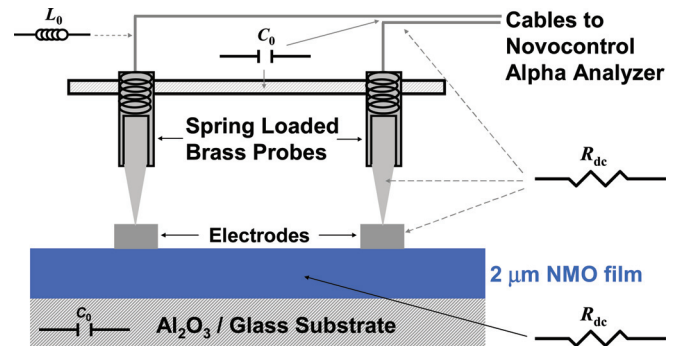


FIG. 4. (Color online) Experimental set-up for the in-plane impedance spectroscopy measurements for NMO films. The equivalent circuit elements R_{dc} , C_0 , and L_0 are depicted, and their origins are indicated.

each IS measurement under open circuit conditions. In the experimental set-up used in this study, a very typical value of $C_0 \approx 5 \times 10^{-13}$ F was determined.

The fact that the circuit component C_0 is parallel to the sample [Fig. 3(a)] can have serious consequences, and 3 possible scenarios exist:

- (1) If C_0 is considerably smaller than C_1 and C_2 , it has no perceptible effect on the impedance spectroscopy data, and C_0 can be neglected and excluded from the circuit. In this ideal case, the dielectric relaxations R_1C_1 and R_2C_2 can usually be deconvoluted readily and analyzed separately.
- (2) In the case where C_0 is significantly larger than C_1 and C_2 , C_0 totally dominates the IS data, and C_1 and C_2 cannot be obtained. The dielectric relaxations R_1C_1 and R_2C_2 cannot be deconvoluted, and the equivalent circuit “collapses” to one single RC element as illustrated by the circuit in Fig. 3(b). As a consequence, the two resistors R_1 and R_2 cannot be separated, and the IS data show the features of only 1 resistor [in Fig. 3(b), this is shown as R_{1+2}], representing the sum of R_1 and R_2 , and one capacitor representing the stray capacitance (C_0). The single resistor accounts for the total resistance of the sample and, therefore, corresponds to the dc resistance.
- (3) If C_0 is comparable to C_1 and C_2 , the situation is more complicated. Under certain circumstances, it might be possible to determine C_1 and C_2 by employing the equivalent circuit shown in Fig. 3(a). In other cases, it might be possible to determine only C_2 by omitting C_1 in the circuit in Fig. 3(a).

In order to predict which of the above scenarios will apply to a given sample, the value for the intrinsic capacitance C_1 (bulk) needs to be estimated and compared to the stray capacitance C_0 determined from open circuit measurements. Such estimations for C_1 can be obtained from the well-known equation for capacitance: $C = \epsilon_r \epsilon_0 (A/d)$, where A is the current cross section and d is the electrode distance. The factor A/d is usually referred to as the geometrical factor g . By comparing the in-plane and out-of-plane film and bulk IS measurements, it is obvious that g can strongly influence the expected capacitance C_1 . The situations for in-plane and out-of-plane film and for bulk sample measurements can in fact be quite different:

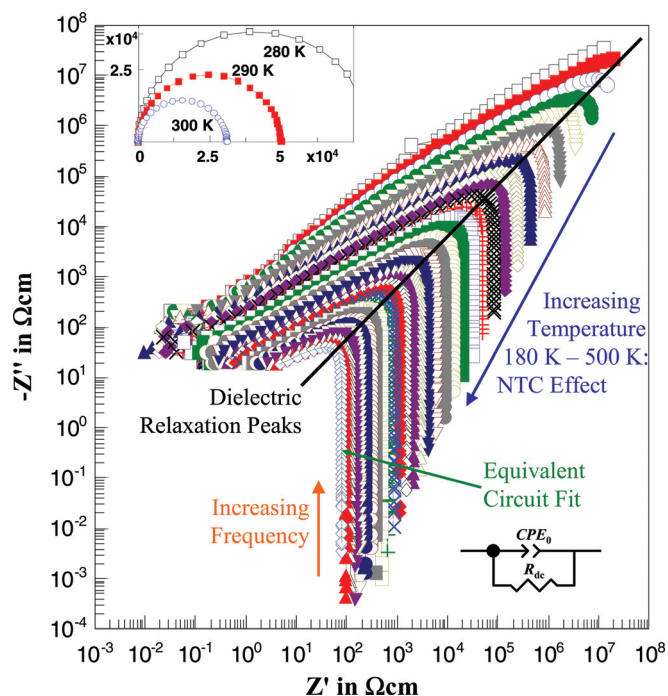


FIG. 5. (Color online) Complex impedance plots of $-Z''$ vs Z' , both in Ωcm , on double-logarithmic axes for an annealed NMO film on Al_2O_3 . All other films investigated show equivalent behavior. The data curves were taken at 180–500 K at 10 K intervals. The NTC effect is indicated, and an equivalent circuit fit is shown for the data collected at 500 K by the thin solid line. Inset: Plots of $-Z''$ vs Z' (Ωcm) on linear axes for 280, 290, and 300 K displaying one single quasi-ideal semicircle each.

- (i) For out-of-plane film IS measurements, A (electrode area) is usually macroscopic, whereas d (film thickness) is microscopic. This leads to large g and C_1 values. Because the extrinsic capacitance C_2 is expected to be larger than C_1 , scenario (1) may well apply here.⁴⁶
- (ii) For in-plane film IS measurements, A (electrode width \times film thickness) is usually microscopic and d (electrode distance) is macroscopic, leading to small g and C_1 values. In most cases, scenario (2) applies here. In the case in which C_2 appears to be larger than C_0 , scenario (3) applies. It should be noted that A is an estimate only, because the current cross section is not clearly defined for co-planar electrodes in in-plane film measurements.
- (iii) For bulk IS measurements, A (electrode area) is usually macroscopic and d (electrode distance) is macroscopic as well, which leads to g values on the order of 1 and to intermediate C_1 values, often similar to C_0 . C_2 is usually larger than C_0 here, and scenario (1) or (3), depending on the exact values, may be applicable.⁴³

C. In-plane IS measurements in AD NiMn_2O_4 films

For a rough approximation of the intrinsic film capacitance C_1 for our in-plane IS measurements on NTC thermistor films, we used the NMO bulk value for ϵ_r (Ref. 21), and we calculated a g value of $\approx 5 \times 10^{-4} \text{ cm}$ from the sample geometry, which leads to a C_1 value of approximately $3 \times 10^{-16} \text{ F}$. This C_1 , as well as a possible extrinsic GB capacitance C_2 ,²¹ would be considerably smaller than C_0 . Elec-

trode sample interface contributions were not indicated for our films, and scenario (1) and the circuit in Fig. 3(b) were applied.

However, our IS data showed clear features indicating that C_0 was not ideal, and a small degree of nonideality was evident, which could be accounted for by replacing C_0 with a CPE.⁴² In Fig. 3(c), the circuit is modified accordingly, the nonideal capacitance is represented by CPE_0 , and the dc resistance of the film is represented by R_{dc} .

Figure 4 illustrates the experimental setup for in-plane IS measurements, and the equivalent circuit elements are depicted according to their origin. For the sake of completeness, it should be noted that the inductance of the measurement cables can have an influence on the IS data, which can be accounted for by a series inductor L_0 . Such inductive influences can occur at high frequency, if the impedance is small. L_0 was neglected in our study here because no inductive behavior was obvious from the spectra, and L_0 was therefore not included in the circuit in Fig. 3. Additionally, it should be noted that R_{dc} may contain contributions from the cable, pin, and electrode resistance (Fig. 4), but such contributions were found to be negligible here from short circuit measurements. For in-plane measurements C_0 can contain contributions from the substrate, which is also indicated in Figure 4.

IV. RESULTS AND DISCUSSION

A. Impedance spectroscopy data analysis

IS data were obtained for NMO 2 μm thick films on glass and for Al_2O_3 substrates in the as-deposited state and after annealing in air at 600 $^\circ\text{C}$ (glass) or 850 $^\circ\text{C}$ (Al_2O_3). Figure 5 shows plots of the imaginary versus the real part of the complex impedance ($-Z''$ vs Z') for annealed films on Al_2O_3 . The data are plotted on double-logarithmic axes, and therefore the almost perfect single semicircles at each temperature appear distorted. The maximum in $-Z''$ represents the relaxation peak of the single dielectric relaxation process detected. No electrode, GB, or bulk relaxations could be

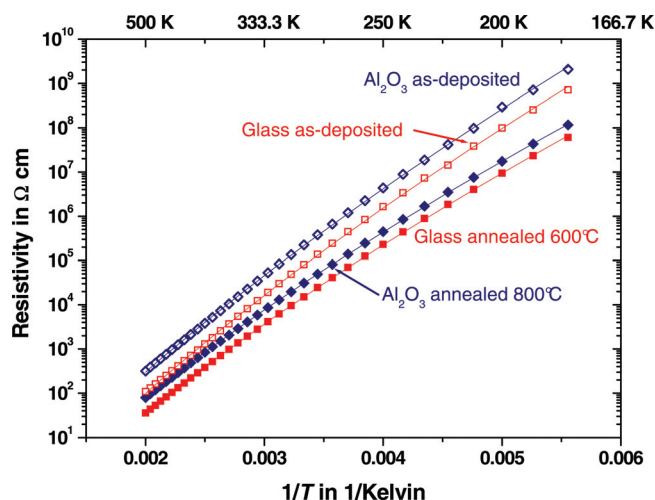


FIG. 6. (Color online) Arrhenius plots of the logarithmic dc resistivity ρ (Ωcm) vs the reciprocal temperature $1/T$ (1/Kelvin) at 180–500 K for NMO films on glass [as-deposited (\square) and annealed (\blacksquare)] and on Al_2O_3 [as-deposited (\diamond) and annealed (\blacklozenge)]. Solid lines represent fits to Eq. (1).

TABLE I. Variable range hopping parameters p , T_0 , C , and $g(0.15 \text{ eV})$ from fits of the ρ - T data to the model in Eq. (1).

	p	T_0 (K)	C ($\Omega\text{cm}/\text{K}^{2p}$)	$g(0.15 \text{ eV})$ ($\text{eV}^{-1}\text{cm}^{-3}$)
As-deposited Al_2O_3	0.626 ± 0.011	$5.60 \times 10^4 \pm 4 \times 10^3$	$6.07 \times 10^{-10} \pm 1 \times 10^{-10}$	5.6×10^{-19}
As-deposited glass	0.600 ± 0.015	$7.59 \times 10^4 \pm 8 \times 10^3$	$8.71 \times 10^{-11} \pm 3 \times 10^{-11}$	7.8×10^{-19}
Annealed Al_2O_3	0.586 ± 0.003	$7.50 \times 10^4 \pm 2 \times 10^3$	$3.58 \times 10^{-10} \pm 3 \times 10^{-11}$	2.0×10^{-20}
Annealed glass	0.581 ± 0.005	$8.15 \times 10^4 \pm 3 \times 10^3$	$1.04 \times 10^{-10} \pm 1 \times 10^{-11}$	1.9×10^{-20}

deconvoluted as explained in Secs. III B and III C due to the dominance of the stray over the NMO in-plane film capacitance. From Fig. 5, it is clear that Z' is frequency independent at sufficiently low frequencies at the vertical parts of each curve. The frequency independent Z' values correspond to the resistance R_{dc} and, therefore, represent the dc resistivity of the film. The film dc resistivity drops with increasing temperature, which is the typical NTC behavior of NMO thermistor materials. For the highest temperature (500 K), the fit to the equivalent circuit model [Fig. 3(c)] is shown (solid curve) and exhibits perfect agreement with the data. The fits to the data at all remaining temperatures are equally convincing. The critical CPE exponent n was very close to 1 at all temperatures in the range of 0.97–1, as is expected for an almost perfect Debye behavior of a parasitic contribution. The data for all other AD film samples display the equivalent features and could be fitted to the same equivalent circuit equally well.

B. NTC thermistor behavior of the dc film resistivity

Values for R_{dc} were obtained from the fits of the IS data to the equivalent circuit model shown in Fig. 3(c)/Fig. 5 and were plotted as the resistivity ρ on a logarithmic axis versus the reciprocal temperature T on Arrhenius axes (Fig. 6). The ρ - T curves for all samples show good uniformity over the full temperature range of 180 K to 500 K and exhibit the typical bending for VRH. The strict uniformity of the ρ - T curves over a large temperature range is a unique property of NTC therm-

istor materials based on NMO spinels and enables the application of these materials in wide range temperature sensors.

The as-deposited films show a lesser degree of VRH bending, higher resistivity, and higher activation energy as compared to annealed films. The Arrhenius plots in Fig. 6 were fitted to Eq. (1) using Origin[®] software employing a least-linear square fitting routine with statistical weighting of the residues and a Levenberg-Marquardt algorithm. The solid lines in Fig. 6 represent such fits to the data and show excellent agreement with the data points. The parameters obtained from such VRH fits are summarized in Table I, including the first standard deviation of the fitting uncertainties. It is important to note that the factor T_0 may not be interpreted as an activation energy here, because T_0 is temperature independent in contrast to the temperature dependent activation energy. T_0 is related to the density of localized electron states $g(\epsilon)$ contributing to the hopping process.^{36,37} $g(\epsilon)$ values at $\epsilon = 0.15 \text{ eV}$ above Fermi level ($\epsilon = 0$) were calculated from T_0 and p , and are listed in Table I. The p and $g(0.15 \text{ eV})$ values of the annealed films are in good agreement with bulk NiMn_2O_4 values reported previously.³⁶ In contrast, the as-deposited films show a lower density of localized electron states contributing to the hopping process. Obviously, annealing and concomitantly improved film crystallization bring the charge transport properties of AD films closer to the bulk behavior. In Ref. 36, polycrystalline thick film values are reported as well, but such films contained a glass phase, and the values of single phase NiMn_2O_4 films shown here might be more representative.

The gradients of the Arrhenius plots in Fig. 6 may be interpreted as local activation energies ϵ_3 , which were determined by taking the first derivative of such curves. ϵ_3 values represent the activation energy at one specific temperature only, in contrast to global activation energies E_A . In the context of NTC thermistors, such local activation energies ϵ_3 given in Kelvin are often referred to as the thermistor constant B .⁴⁷ Due to reduced scatter in the ρ - T data, such ϵ_3 or B values show clear trends with temperature, which are plotted in Fig. 7. It is evident that the as-deposited films show higher ϵ_3/B values and a stronger temperature dependence of the resistance than the annealed films. Therefore, as-deposited AD films might offer slightly higher values of the absolute sensitivity to temperature changes. In contrast, the annealed films on Al_2O_3 show the lowest level of data scatter in Fig. 7 and might be favorable in terms of the reliability aspect. The ϵ_3 and B values from IS measurements agree well with the ones from conventional dc measurements.²⁸ A further relevant parameter in NTC thermistor technology is the relative sensitivity B/T , which is shown in the inset of Fig. 7. The relative sensitivity in as-deposited films is higher, in agreement with

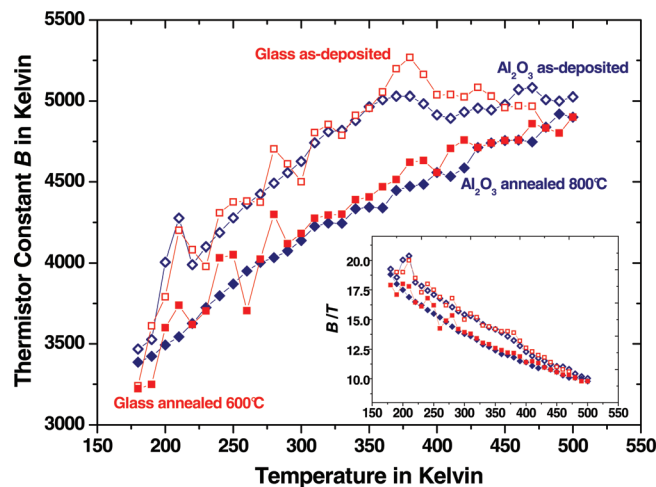


FIG. 7. (Color online) NTC thermistor constants B (Kelvin) vs temperature (Kelvin) obtained from the first derivative of the Arrhenius plots in Fig. 6 for films on glass [as-deposited (\square) and annealed (\blacksquare)] and on Al_2O_3 [as-deposited (\diamond) and annealed (\blacklozenge)]. B corresponds to the local activation energies ϵ_3 (in Kelvin). Inset: Relative sensitivity of the NTC thermistor: B/T (dimensionless) vs temperature (in Kelvin).

the absolute sensitivity B , and slightly decreases with increasing temperature. Such a decrease in relative sensitivity with increasing temperature is expected for NTC thermistor devices.

V. CONCLUSIONS

Films of NTC thermistor NMO material were successfully produced via aerosol deposition and might be applicable in temperature sensing and related applications. Impedance spectroscopy was employed in order to determine precisely the dc resistivity versus temperature (ρ - T) dependence, the local activation energies ϵ_3 , the thermistor constants B , and the relative NTC thermistor sensitivity B/T of all films. In plane ac impedance measurements in NMO films proved to enable more precise resistivity determination over a wider temperature range as compared to conventional dc measurements.²⁸ Therefore, the read-out of the resistivity values from film NTC thermistor temperature sensors in industrial applications might be performed preferably by in-plane low frequency ac fields.

The ρ - T curves for all AD film samples showed the typical NTC thermistor behavior over a large temperature range (180–500 K) and followed a variable-range hopping power-law. As-deposited films showed an increased sensitivity of the resistance to temperature changes. Annealed films deposited on Al₂O₃ showed the lowest scatter in differentiated ρ - T data and might exhibit superior reliability in temperature sensing applications.

ACKNOWLEDGMENTS

The authors wish to thank Carlos León and Alberto Rivera for help using the IS equipment, and the Mechanical Workshops at the Facultad de Ciencias Físicas at the Universidad Complutense de Madrid for technical support. J.R. and D.-S.P. were financially supported by a grant from the Fundamental R&D Program for Core Technology of Materials, funded by the Ministry of Knowledge Economy, Republic of Korea. R.S. wishes to acknowledge the Ministerio de Ciencia e Innovación in Spain for granting a Ramon y Cajal Fellowship.

- ¹J. A. Becker, C. B. Green, and G. L. Pearson, *Bell Syst. Tech. J.* **26**, 170 (1947).
- ²B. Boucher, C. R. Hebd. Seances Acad. Sci. **249**, 514 (1957).
- ³E. G. Larson, R. J. Arnott, and D. G. Wickham, *J. Phys. Chem. Solids* **23**, 1771 (1962).
- ⁴N. Renault, N. Baffier, and M. Huber, *J. Solid State Chem.* **5**, 250 (1972).
- ⁵V. A. M. Brabers and J. C. J. M. Terhell, *Phys. Status Solidi A* **69**, 325 (1982).
- ⁶S. Fritsch, J. Sarrias, M. Brieu, J. J. Couderc, J. L. Baudour, E. Snoeck, and A. Rousset, *Solid State Ionics* **109**, 229 (1998).
- ⁷R. Schmidt, A. Basu, and A. W. Brinkman, *J. Eur. Ceram. Soc.* **24**, 1233 (2004).
- ⁸J. L. M. de Viales, P. Garcia-Chain, R. M. Rojas, E. Vila, and O. Garcia-Martinez, *J. Mater. Sci.* **33**, 1491 (1998).
- ⁹G. D. C. Csete de Gyoergyfalva, A. N. Nolte, and I. M. Reaney, *J. Eur. Ceram. Soc.* **19**, 857 (1999).

- ¹⁰A. Veres, J. G. Noudem, O. Perez, S. Fourrez, and G. Bailleul, *Solid State Ionics* **178**, 423 (2007).
- ¹¹A. Feteira, *J. Am. Ceram. Soc.* **92**, 967 (2009).
- ¹²O. Shpotyuk, A. Kovalskiy, O. Mrooz, L. Shpotyuk, V. Pechnyo, and S. Volkov, *J. Eur. Ceram. Soc.* **21**, 2067 (2001).
- ¹³A. Veres, J. G. Noudem, O. Perez, S. Fourrez, and G. Bailleul, *J. Eur. Ceram. Soc.* **27**, 3873 (2007).
- ¹⁴C. Zhao, B. Wang, P. Yang, L. Winnubst, and C. Chen, *J. Eur. Ceram. Soc.* **28**, 35 (2008).
- ¹⁵D. G. Wickham, *J. Inorg. Nucl. Chem.* **26**, 1369 (1964).
- ¹⁶A. Feltz and J. Töpfer, *Z. Anorg. Allg. Chem.* **576**, 71 (1989).
- ¹⁷J. Jung, J. Töpfer, J. Mürbe, and A. Feltz, *J. Eur. Ceram. Soc.* **6**, 351 (1990).
- ¹⁸R. Schmidt, A. Stiegelschmitt, A. Roosen, and A. W. Brinkman, *J. Eur. Ceram. Soc.* **23**, 1549 (2003).
- ¹⁹Y. Torry, H. Tsuzuki, K. Kato, Y. Uwamino, B. H. Choi, and M. J. Lee, *J. Mater. Sci.* **31**, 2603 (1996).
- ²⁰J. A. Schmidt, A. E. Sagua, J. C. Bazán, M. R. Prat, M. E. Braganza, and E. Morán, *Mater. Res. Bull.* **40**, 635 (2005).
- ²¹A. Díez, R. Schmidt, A. E. Sagua, M. A. Frechero, E. Matesanz, C. León, and E. Morán, *J. Eur. Ceram. Soc.* **30**, 2617 (2010).
- ²²F. Lindner and A. Feltz, *J. Eur. Ceram. Soc.* **11**, 269 (1993).
- ²³S. Baliga and A. L. Jain, *Mater. Lett.* **8**, 175 (1989).
- ²⁴P. Fau, J. P. Bonino, J. J. Demai, and A. Rousset, *Appl. Surf. Sci.* **65/66**, 319 (1993).
- ²⁵A. Ikegami, *IEEE Trans. Compon., Hybrids, Manuf. Technol.* **3**, 541 (1980).
- ²⁶R. Schmidt, A. Basu, A. W. Brinkman, Z. Klusek, W. Kozłowski, P. K. Datta, A. Stiegelschmitt, and A. Roosen, *Appl. Surf. Sci.* **252**, 8760 (2006).
- ²⁷A. Basu, A. W. Brinkman, and R. Schmidt, *J. Eur. Ceram. Soc.* **24**, 1247 (2004).
- ²⁸J. Ryu, K.-Y. Kim, J.-J. Choi, B.-D. Hahn, W.-H. Yoon, B.-K. Lee, D.-S. Park, and C. Park, *J. Am. Ceram. Soc.* **92**, 3084 (2009).
- ²⁹K. Park and D. Y. Bang, *J. Mater. Sci.: Mater. Electron.* **14**, 81 (2003).
- ³⁰H. Schulze, J. Li, E. C. Dickey, and S. Trolier-McKinstry, *J. Am. Ceram. Soc.* **92**, 738 (2009).
- ³¹S. W. Ko, J. Li, N. J. Podraza, E. C. Dickey, and S. Trolier-McKinstry, *J. Am. Ceram. Soc.* **94**, 516 (2011).
- ³²R. Schmidt, A. Basu, A. W. Brinkman, Z. Klusek, and P. K. Datta, *Appl. Phys. Lett.* **86**, 073501 (2005).
- ³³S. Baliga and A. L. Jain, *Mater. Lett.* **11**, 226 (1991).
- ³⁴Y. Hou, Z. Huang, Y. Gao, Y. Ge, J. Wu, and J. Chu, *Appl. Phys. Lett.* **92**, 202115 (2008).
- ³⁵J. Wu, Z. Huang, Y. Hou, Y. Gao, and J. Chu, *Appl. Phys. Lett.* **96**, 082103 (2010).
- ³⁶R. Schmidt, A. Basu, and A. W. Brinkman, *Phys. Rev. B* **72**, 115101 (2005).
- ³⁷B. I. Shklovskii and A. L. Efros, *Electronic Properties of Doped Semiconductors* (Springer - Verlag, Berlin, 1984).
- ³⁸R. Schmidt and A. W. Brinkman, *J. Appl. Phys.* **103**, 113710 (2008).
- ³⁹W. Chen, W. Zhu, O. K. Tan, and X. F. Chen, *J. Appl. Phys.* **108**, 034101 (2010).
- ⁴⁰A. Srivastava, A. Garg, and F. D. Morrison, *J. Appl. Phys.* **105**, 054103 (2009).
- ⁴¹M. Li, A. Feteira, and D. C. Sinclair, *J. Appl. Phys.* **105**, 114109 (2009).
- ⁴²Impedance Spectroscopy: Theory, *Experiments and Applications*, edited by E. Barsoukov and J. R. Macdonald (John Wiley & Sons, New York, 2005).
- ⁴³J. T. S. Irvine, D. C. Sinclair, and A. R. West, *Adv. Mater.* **2**, 132 (1990).
- ⁴⁴R. Schmidt, in *Ceramic Materials Research Trends*, edited by P. B. Lin (Nova Science Publishers, New York, 2007).
- ⁴⁵C. H. Hsu and F. Mansfeld, *Corros. Sci.* **57**, 747 (2001).
- ⁴⁶R. Schmidt, W. Eerenstein, T. Winiecki, F. D. Morrison, and P. A. Midgley, *Phys. Rev. B* **75**, 245111 (2007).
- ⁴⁷E. D. Macklen, *Thermistors* (Electrochemical Publications, Glasgow, 1979).